EDGE ARTICLE

Topochemical photocycloaddition in two-dimensional lead-halide coordination polymers with tunable phosphorescence

Zhongwei Chen,[a] Jin Wu, [ID][a] Zeyu Deng, [ID]*[b] Congcong Chen,[c] Jianning Feng,[a] Baixu Ma,[c] Lizhi Tao, [ID][c] Lingling Mao [ID][c] and Haipeng Lu [ID]*[a]

Topochemical transformation in which the parent structural motifs are preserved has become a powerful strategy to access new advanced materials. Solid-state topochemical conversion in a single-crystal-to-single-crystal (SCSC) fashion is particularly attractive as it provides design principles with unequivocal structural details. Here, we report a series of two-dimensional (2D) lead-halide coordination polymers with bipyridyl ethylene (bpe) ligands that can undergo quantitative SCSC [2 + 2] photocycloaddition. The chemical and structural diversity of 2D lead-halide coordination polymers allows systematic modulation of the rate of SCSC [2 + 2] photocycloaddition by changing the halide and bpe ligands. Our work reveals the structure–property relationship in lead-halide coordination polymers during the dynamic [2 + 2] photocycloaddition process. The photo-transformed coordination polymers with cyclobutane linkages show drastically different properties in optical absorption and emission. We present a viable strategy to modify the structure and properties of lead-halide coordination polymers by post-synthetic modification.

Introduction

Topochemical transformation of solid-state reactions within confined crystal lattices offers a powerful strategy to access complex molecules with chemoselectivities that are otherwise unattainable with solution methods. When the conversion is at the single-crystal-to-single-crystal (SCSC) level,[1,2] the exact structural change upon conversion can be unequivocally determined by single-crystal X-ray diffraction (SCXRD), thus offering an ideal system to probe chemical reactions at the atomic level. These conversions are generally triggered by external stimuli, such as heat or light.[3–6] During the dynamic conversion, new molecules and structural motifs are generated, and the entire process can be arrested and probed by spectroscopic and structural techniques.

In particular, solid-state [2 + 2] photocycloaddition has emerged as a versatile topochemical reaction owing to the diverse substrates (*e.g.*, diarylethene,[7,8] cyanostilbene,[9,10] and benzo-heterocycle[11,12]) and the (semi-)quantitative nature. The main requirement for the solid-state photocycloaddition is generally described by Schmidt's rule,[13] which defines the longest distance of the neighboring parallel double bonds for [2
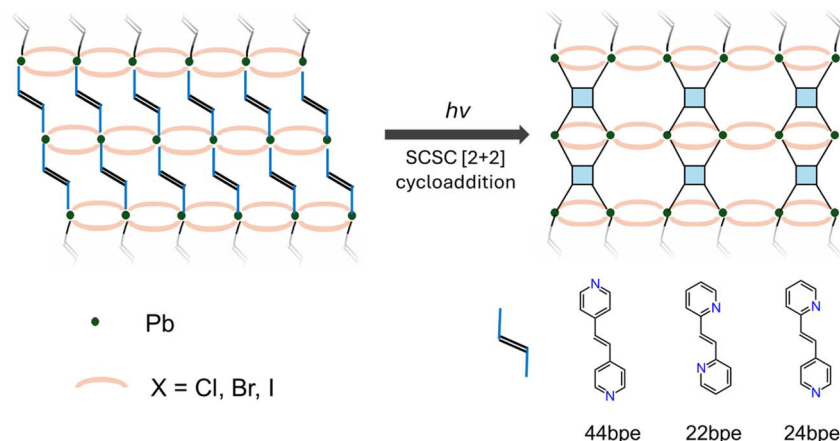
+ 2] photocycloaddition to be 4.2 Å. Specifically, [2 + 2] photocycloaddition occurs efficiently only when molecules with double bonds are packed in parallel within a distance of 4.2 Å. However, the complicated interplay between distance, geometry, and morphology remains to be fully understood.[14–16] SCSC [2 + 2] photocycloaddition has been demonstrated in a variety of organic polymers and hybrid materials, including metal–organic frameworks (MOFs),[17,18] covalent organic frameworks (COFs),[19,20] and other coordination polymers (CPs),[21–23] enabling new properties such as photochromism[24–29] and the photo-salient effect.[27,30–34]

Metal-halide coordination polymers (CPs) contain inorganic metal-halide building blocks that are connected by organic linkers through coordination bonds.[35–37] The robust covalent bonds grant metal–halide CPs outstanding structural rigidity and stability when compared to conventional ionic metal-halide perovskites. Furthermore, heavy metal halides display strong spin–orbit coupling (SOC), which promotes the spin-forbidden intersystem crossing (ISC), leading to long-lived phosphorescence.[38,39] A number of metal-halide CPs, including zinc-halide,[40–42] bismuth-halide,[43] and lead-halide[22,44] CPs have been shown to undergo quantitative [2 + 2] photocycloaddition, and their structure and properties were modulated upon conversion. However, the key structure–property relationship that governs the rate and effect of photocycloaddition remains unknown, stemming from the lack of a systematic study in metal-halide CPs. Lead-halide CPs have recently attracted much attention because of their interesting optoelectronic and enhanced stability.[36,37,45,46] The Pb atoms have strong

a Department of Chemistry, The Hong Kong University of Science and Technology, Kowloon, Hong Kong (SAR) 999077, China. E-mail: haipenglu@ust.hk

b Department of Materials Science and Engineering, National University of Singapore, Singapore 117575, Singapore. E-mail: msedz@nus.edu.sg

c Department of Chemistry, Southern University of Science and Technology, Shenzhen, 518055, China

Scheme 1 Schematic illustration for the design of lead halide coordination polymers and their solid-state [2 + 2] photocycloaddition process.

coordination ability with N and O in the organic ligands, enabling a large structural library for the hybrid lead-halide CPs. Designing lead-halide CPs with photo-responsive bpe ligands provides an unusual strategy to regulate their optical properties by external stimuli.

In this work, we present such an investigation on the SCSC [2 + 2] photocycloaddition by synthesizing a series of lead-halide CPs. As shown in Scheme 1, three bipyridyl ethylene (bpe) molecules, 1,2-bis(4-pyridyl)ethylene (44bpe), 1,2-bis(2-pyridyl) ethylene (22bpe), and (E)-2-[2-(pyridin-4-yl)vinyl]pyridine (24bpe), were selected for constructing lead-halide CPs, bpe-PbX$_2$ (X = Cl, Br, I). Six lead-halide CPs, namely 44bpe-PbX$_2$ (X = Cl, Br, I), 22bpe-PbBr$_2$, 22bpe-PbI$_2$, and 24bpe-PbI$_2$ were synthesized. These CPs feature two-dimensional (2D) connectivity with different inorganic frameworks. The lead-halide framework acts as a template to arrange the packing of bpe molecules, in which way the intermolecular distance of bpe and packing geometry can be modulated via the Pb–N coordination geometry. Our results show that both the intermolecular double bond distance and the absorption can affect the photocycloaddition reactivity. Additionally, the different packing modes of bpe molecules result in various stereoselective cyclobutane products, indicating the potential for precise synthesis through solid-state photocycloaddition. The SCSC topochemical transformation was confirmed by solving the single crystal structures of the photoproducts. More importantly, we show that the quantitative [2 + 2] photocycloaddition further modulates the optoelectronic properties of lead-halide CPs. Our work presents a strategy to modify the structure and properties of these bpe-based lead-halide CPs and unveils the structure–property relationships that govern the optical properties in this process.

Results

Synthesis and crystal structures of 2D lead-halide coordination polymers

The bpe-based lead-halide CPs were synthesized by the thermogradient method from a MeOH/H$_2$O solution (Experimental section). Six bpe-PbX$_2$ CPs were successfully synthesized,

namely, 44bpe-PbX$_2$ (X = Cl, Br, I), 22bpe-PbBr$_2$, 22bpe-PbI$_2$, and 24bpe-PbI$_2$. Notably, five of them are reported for the first time. 44bpe-PbBr$_2$ was previously reported;[47] however, the SCSC topochemical conversion remains unknown. Crystal structures of these six compounds were determined by SCXRD (Fig. 1 and S1). Crystallographic data and structure refinement information appear in Table S1 (CCDC no. 2407139 and 2407230–2407233). The phase purity of these CPs was further confirmed by powder X-ray diffraction (PXRD) (Fig. S2).

In general, these lead-halide CPs display 2D connectivity (Fig. 1) with rich structural diversity. The inorganic component consists of 1D lead-halide chains, which are then crosslinked by the bpe ligands through the Pb–N coordination bonds. Each Pb^{2+} forms an octahedron with two N from the bpe ligands and four halide ions. Different bpe isomers lead to different coordination geometries and Pb–X chain structures. There are two types of Pb–X chain structures in these bpe-PbX$_2$ CPs. Here, five of these CPs (44bpe-PbX$_2$ (X = Cl, Br, I), 22bpe-PbBr$_2$, and 24bpe-PbI$_2$) show 1D linear Pb–X chains, which consist of edge-sharing [PbX$_4$N$_2$] octahedra (Fig. 1, type-I). However, 22bpe-PbI$_2$ shows 1D corrugated Pb–X chains (Fig. 1, type-II). These 1D Pb–X chains are then interconnected by the bpe ligands through the Pb–N coordination bonds. These lead-halide CPs show superior stability in air and solvent (Fig. S3).

Interestingly, the exact position of N in bpe isomers has a direct impact on the coordination geometry and the 2D framework structure. For instance, in 44bpe-PbX$_2$ series (X = Cl, Br, I), each Pb^{2+} is coordinated with four halides in the equatorial plane and two N in the axial position (Fig. 1a, e, and S1). The crystal structure of 44bpe-PbX$_2$ shows a planar 2D structure, where 44bpe molecules are in parallel positions. The distance between the adjacent double bonds is determined by the Pb–$^\mu$X–Pb distance in the 1D chain, which is shown to be 4.05, 4.19, and 4.36 Å for X = Cl, Br, and I, respectively. The larger the halide ions, the longer the adjacent double bond distance.

In the 22bpe-PbBr$_2$ CP (Fig. 1b and f), the coordination geometry of 22bpe results in the formation of a wrinkled 2D framework consisting of 1D linear Pb–Br chains interconnected
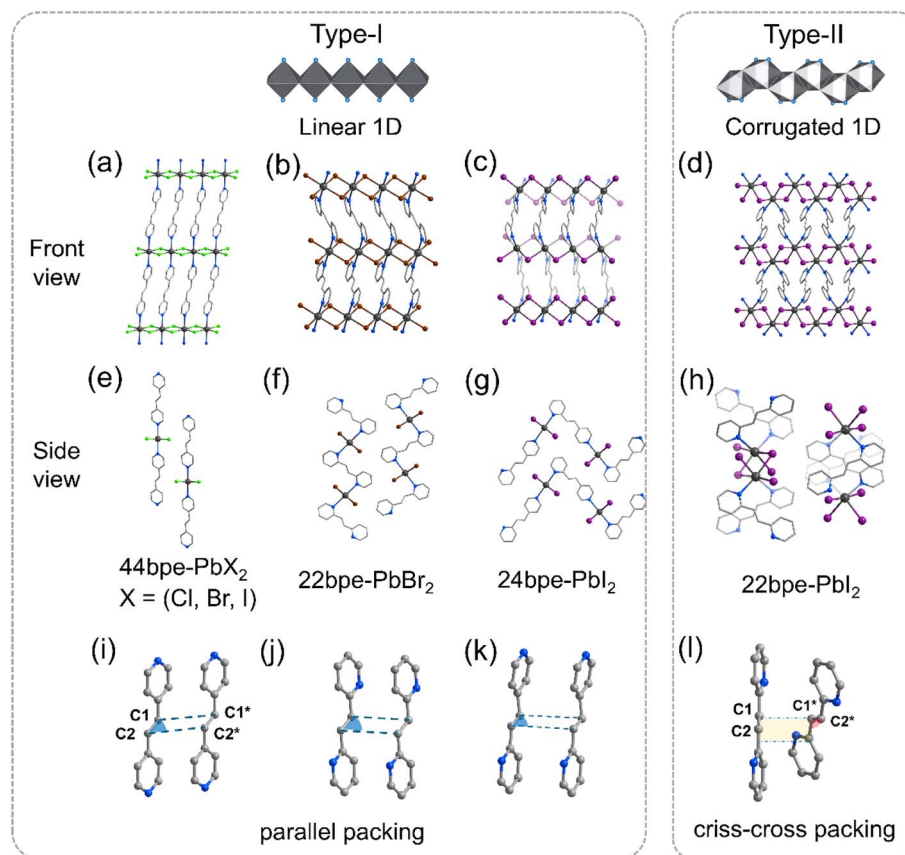
Fig. 1 Structures of bpe-based lead-halide CPs. (a–d) Front view of the 2D structures of 44bpe-PbX$_2$ (X = Cl, Br, I), 22bpe-PbBr$_2$, 24bpe-PbI$_2$, and 22bpe-PbI$_2$. (e–h) Side view of the 2D structures of 44bpe-PbX$_2$, 22bpe-PbBr$_2$, 24bpe-PbI$_2$, and 22bpe-PbI$_2$. (i–k) Parallel packing of 44bpe, 22bpe, and 24bpe. (l) Criss-cross packing of 22bpe. Green, blue, brown, purple, and dark spheres denote the Cl, N, Br, I, and Pb atoms, respectively. Gray sticks denote the C atoms.

with the 22bpe ligands. The adjacent 22bpe ligands pack in parallel with a double bond distance of 4.13 Å, similar to that in 44bpe-PbBr$_2$. This kind of wrinkled 2D structure is also formed in 24bpe-PbI$_2$ (Fig. 1c and g) with similar 1D linear Pb–I chains. The 24bpe ligands also pack in parallel in the 24bpe-PbI$_2$ CP with a double bond distance of 4.34 Å.

However, the structure of 22bpe-PbI$_2$ varies significantly from other 2D CPs (Fig. 1d and h). In this structure, each Pb^{2+} is coordinated with two N at the adjacent equatorial position of the octahedron, forming the corrugated [PbI$_4$N$_2$] chains. The Pb–I chains are then connected by the 22bpe ligands to form 2D frameworks. Here, the 22bpe ligands are criss-cross packed within the 2D framework (Fig. 1l).

In addition to the different inorganic frameworks, the geometry of bpe ligands also varies significantly in these CPs. For instance, in the type-I structure, all adjacent bpe ligands are packed in parallel with tunable intermolecular distance and packing geometry (Fig. 1i–k). The two adjacent bpe molecules align face-to-face with different slippage angles. The degree of overlapping can be described by $\angle$C1–C2–C2*. This value is between 58° and 60° in the 44bpe-PbX$_2$ series, which increased to 68.0° and 79.3° in 22bpe-PbBr$_2$ and 24bpe-PbI$_2$ CPs, respectively. The larger the $\angle$C1–C2–C2*, the greater the orbital

overlapping in adjacent bpe ligands. In the type-II structure, two adjacent bpe ligands are not packed in parallel, and the dihedral angle $\angle$C2–C1–C1*–C2* was measured to be 41° (Fig. 1l). To facilitate the [2 + 2] photocycloaddition, the bpe ligands would need to twist and rotate in 22bpe-PbI$_2$ CPs. The adjacent double bond distance and overlapping angles in all bpe-PbX$_2$ CPs are summarized in Table 1. Therefore, the rich chemical and structural diversity of these bpe-PbX$_2$ CPs provides an ideal platform to investigate the impact of intermolecular bond distance, overlapping angles, and packing geometry on the SCSC [2 + 2] photocycloaddition reactions.

Table 1 Structure parameters of the packed bpe molecules

	d_{C1-C1*} (Å)	$\angle$C1–C2–C2* (°)	$\angle$C2–C1–C1*–C2* (°)
44bpe-PbCl$_2$	4.05	58.4	0 (Parallel)
44bpe-PbBr$_2$	4.19	59.7	
44bpe-PbI$_2$	4.36	59.5	
22bpe-PbBr$_2$	4.13	68.0	
24bpe-PbI$_2$	4.34	79.3	
22bpe-PbI$_2$	d_{C1-C1*} = 3.68 Å	74.7	41 (Criss-cross)
	d_{C2-C2*} = 3.97 Å		

Quantitative single-crystal-to-single-crystal [2 + 2] photocycloaddition

To study the SCSC [2 + 2] photocycloaddition in these lead-halide CPs, we first characterized their optical properties. UV-vis absorption spectra of lead-halide CPs are shown in Fig. 2a, which show a continuous red-shift from the Pb–Cl to Pb–Br and Pb–I series. This halide-dependent bandgap is ascribed to the charge transfer from the halide ions to organic ligands, that is, halide-to-ligand charge transfer (XLCT).[35,45,48] When changing bpe ligands within the same halide, e.g., Pb–Br or Pb–I series, there is a red-shift of the absorption spectra from the 22bpe and 24bpe to 44bpe series. The smaller bandgap in the 44bpe-PbX$_2$ series indicates that the planar 2D structures are more favorable for the XLCT. The extended bandgaps into the visible range further allow us to trigger the photoreaction with visible light illumination, rather than UV excitation as reported in most literature studies.[22,30,49] Meanwhile, the tunable bandgap of lead-halide CPs offers an additional knob to modulate the photocycloaddition rate.

Here, lead-halide CP microcrystals were irradiated under a Xe lamp (350–850 nm) (Fig. S4 and S5) with a fixed power for different durations, and the photocycloaddition process was monitored by ^{1}H NMR. The products of the lead-halide CPs (bpe-PbX$_2$) are correspondingly denoted as bpe-PbX$_2$-P. After photoirradiation, the photocycloaddition products were analyzed by dissolving the microcrystals in d_6-DMSO. As shown in Fig. 2b, the photoproducts of 44bpe-PbCl$_2$ show a decreasing signal at 7.5, 7.6, and 8.6 ppm under illumination, corresponding to the vinyl and pyridine groups of bpe, respectively. Concurrently, three new peaks at 4.7, 7.2, and 8.3 ppm

corresponding to the cyclobutane ring and pyridine groups on the photocycloaddition product, i.e., rctt-tetrakis(4-pyridyl) cyclobutane (rctt-44-tpcb), appear, suggesting a quantitative [2 + 2] photocycloaddition. The conversion yield can be readily calculated by integration of the NMR peaks. Fig. S5 shows the conversion yield as a function of time in different bpe-PbX$_2$ CPs. Here we define the conversion rate as $1/\tau_{1/2}$, where $\tau_{1/2}$ refers to the time when the conversion yield reaches 50%. Fig. 2c and d show the conversion rate as a function of the double-bond distance and optical bandgap, respectively. In general, the conversion rate roughly increases linearly with the decrease of intermolecular distance, with the exception of type-II 22bpe-PbI$_2$ crystals (Fig. 2c), which feature criss-cross packing of bpe ligands. 44bpe-PbCl$_2$ exhibits the fastest photocycloaddition rate due to the shortest double bond distance. This is in agreement with the commonly reported Schmidt's rule. Meanwhile, the conversion rate increases with the decrease of band gap (Fig. 2d). The bpe-PbI$_2$ series shows a faster reaction rate than the bpe-PbBr$_2$ series, as the broad absorption spectrum in the bpe-PbI$_2$ series is favorable for the absorption of visible light. There is a competing effect between the distance and bandgap on the photocycloaddition rate (Fig. S6). The photocycloaddition rates in these 2D lead-halide CPs are still lower compared to the reported 1D CPs,[22,44] as the 2D framework possesses enhanced connectivity between bpe ligands and lead halides, which restrains the movements of bpe ligands and therefore slows down the photocycloaddition rate.

It should be noted that the generated tetrakis(4-pyridyl) cyclobutane (tpcb) molecules have four steric isomers (Fig. S7). Interestingly, ^{1}H NMR results indicate that when bpe ligands
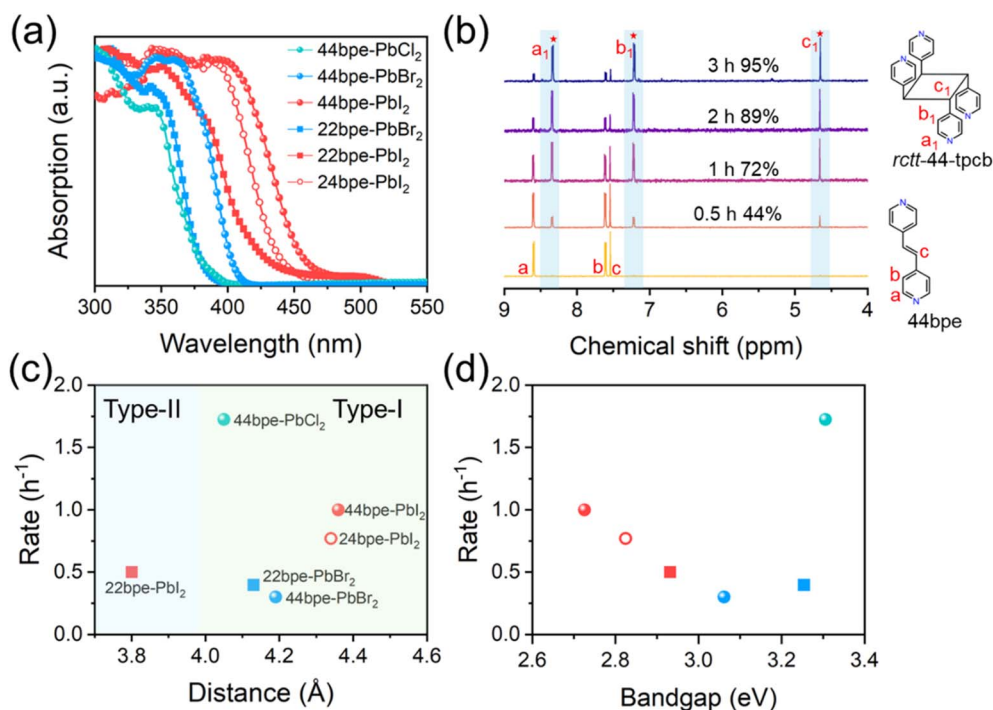

Fig. 2 (a) Absorption spectra of the bpe–PbX$_2$ CPs. (b) ^{1}H NMR spectra of 44bpe–PbCl$_2$ under different irradiation times. (c) Photocycloaddition rates of the bpe–PbX$_2$ CPs with different double bond distances. (d) The relationship between the photocycloaddition rates and bandgap.
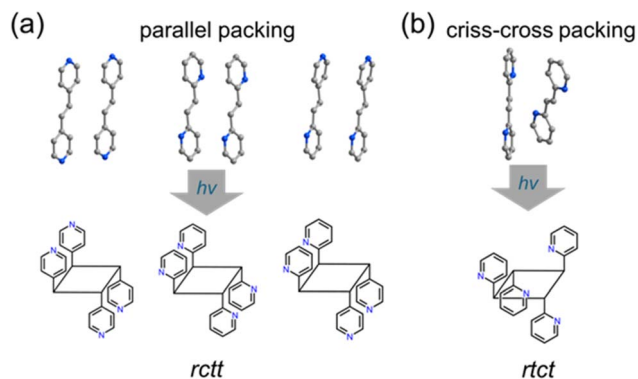
Fig. 3 Different conformations of cyclobutane photoproducts. (a) *rctt*. (b) *rtct*.

are packed in parallel in the type-I structure (44bpe-PbX$_2$, 22bpe-PbBr$_2$, and 24bpe-PbI$_2$), the photocycloaddition products are all in the *rctt* conformation (Fig. 3a and S8–S11). The absolute configuration is further confirmed by the SCXRD result (*vide infra*). However, the photocycloaddition product from the type-II structure (22bpe-PbI$_2$) yields another conformation (Fig. 3b and S10b), that is the *rtct*-22-*tpcb* product.[50] This stereoselective synthesis of the cyclobutane photoproducts originates from the packing mode of bpe ligands. The movement of bpe molecules in lead halide CPs is constrained by the coordination bond, resulting in a spatially closest transition state and yielding stereoselective cyclobutane photoproducts (Fig. 3). The stereoselectivity enabled by the tunable CPs represents a unique opportunity for precision chemistry through the solid-state [2 + 2] photocycloaddition.

Since the photoconversion is carried out in a SCSC fashion, the detailed structural change of CPs upon photocycloaddition

can be precisely determined by SCXRD. The crystal structures of five photoproducts from type-I CPs, namely, 44bpe-PbX$_2$-P (X = Cl, Br, I), 22bpe-PbBr$_2$-P, and 24bpe-PbI$_2$-P, were successfully solved (Table S2, CCDC no. 2407234–2407238). However, the crystal structure of the photoproduct from type-II CPs cannot be solved with high fidelity, likely due to the complicated distortion of the organic ligands. The PXRD data confirm their phase purity after photocycloaddition (Fig. S12). In general, crystal structures of photoproducts display a significant disorder in the organic cyclobutane components (Fig. S13). To better illustrate the structure change, we extracted one set of organic components. As shown in Fig. 4, all bpe molecules are transformed into the corresponding cyclobutane products upon irradiation, indicating a quantitative SCSC photocycloaddition. The absolute configuration of the cyclobutane products can be unequivocally determined as *rctt*, consistent with their NMR data. We have carried out reciprocal space reconstructions (rsr) on 44-bpe-PbCl$_2$ before and after irradiation to monitor the dynamic photocycloaddition process (Fig. S14–S17). It indicates that the initial phase will gradually transfer to the intermediate twin-like cell and to the fully converted photoproduct at the end.

Interestingly, most CPs display minimal changes in their inorganic subunits after photocycloaddition, with the exception of 44bpe-PbCl$_2$-P. In this case, the photocycloaddition induces a spatial shift of the bpe ligands, altering the coordination geometry of the Pb–Cl chains. Specifically, two pyridine units in the *tpcb* ligands move between two adjacent Pb ions (Fig. 4a), resulting in an elongated Pb–N distance of 2.83 Å. This significant structural change arises from the rotation and reorganization of the bpe ligands during the photocycloaddition process. As a result, 44bpe-PbCl$_2$-P exhibits a pronounced photosalient effect (Fig. 4a), causing the crystals to split or bend upon photoirradiation. In contrast, no notable photosalient
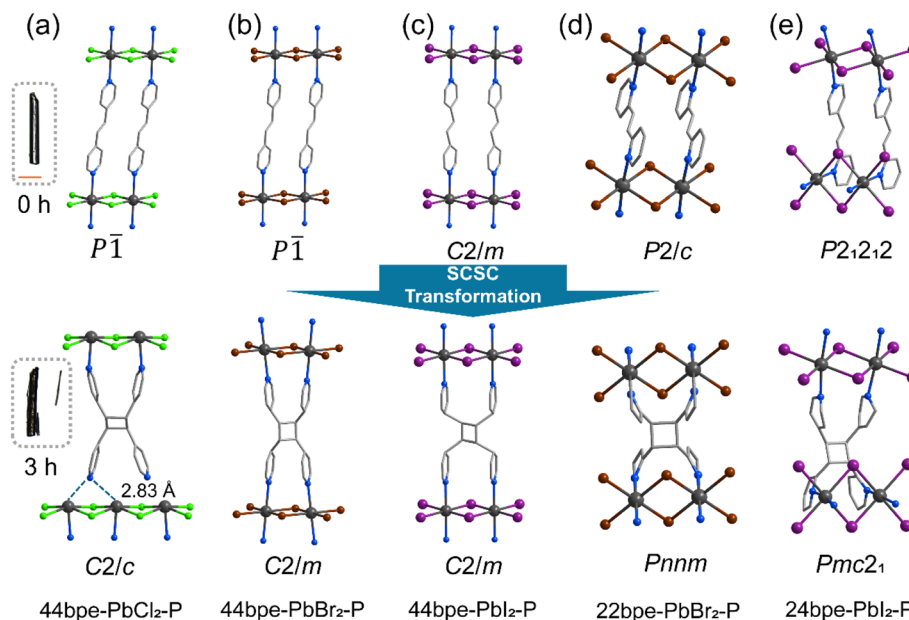

Fig. 4 [2 + 2] Photocycloaddition induced SCSC transformation in bpe-PbX$_2$ CPs. (a) 44bpe-PbCl$_2$-P; the inset shows the single crystal after illumination, scale bar is 100 μm. (b) 44bpe-PbBr$_2$-P. (c) 44bpe-PbI$_2$-P. (d) 22bpe-PbBr$_2$-P. (e) 24bpe-PbI$_2$-P.

effect was observed in the other CPs (Fig. S18). The relatively slow photocycloaddition process allows these crystals to accommodate the strain while keeping the crystal shape.

The thin layers of 44bpe-PbCl$_2$-P can be exfoliated and characterized by AFM (Fig. S19). The thickness lies in the range from 4 nm to 50 nm, which confirms that a layered structure was formed in the 2D coordination polymer. Considering the crystallographic layer with a thickness of about 8 Å, the 4 nm thin layer consists of about 8 layers of 2D polymers. Thermal gravimetric analysis (TGA) suggests that photocycloaddition products of CPs display an enhanced stability (Fig. S20).

Despite the topochemical conversion nature, the space group of photo-irradiated CPs generally shows a higher symmetry compared to the bpe-based CPs (Fig. 4). For instance, the triclinic $P\bar{1}$ space groups of 44bpe-PbCl$_2$ and 44bpe-PbBr$_2$ transforms into monoclinic $C2/c$ and $C2/m$ space groups after photocycloaddition, respectively. Similarly, 22bpe-PbBr$_2$ crystallizes in the monoclinic $P2/c$ space group, while 22bpe-PbBr$_2$-P transforms into the orthorhombic $Pnnm$ space group. This suggests that the SCSC photocycloaddition process is a symmetry-increasing process. We attribute this symmetry-increasing phenomenon to the enhanced structural symmetry of *tpcb* molecules compared to the bpe molecules. It should be noted that this type of photo-induced phase transition in long-range ordered hybrid materials has rarely been observed.[51] In these 2D lead halide CPs, the connectivity based on coordination bonds renders the structural frameworks sensitive to perturbations from the organic ligands during photocycloaddition. This sensitivity can lead to significant alterations in the material's properties and behaviors, highlighting the intricate relationship between the organic components and the inorganic framework in these hybrid systems.

Tuning photophysical properties *via* topochemical photocycloaddition

To explore the impact of photophysical properties of lead-halide CPs upon topochemical [2 + 2] photocycloaddition, we measured their UV-vis absorption and photoluminescence spectra. In general, photo-irradiated CPs display a red-shifted absorption spectrum compared to their parent CPs (Fig. 5). This is particularly obvious in 44bpe-PbCl$_2$-P, 22bpe-PbI$_2$-P, and 24bpe-PbI$_2$-P, where an absorption tail extending the bandgap is observed. This absorption feature is attributed to the cyclobutane derivative radicals,[25,43] which are induced by the electron transfer from halides to organic ligands. The presence of radicals is further confirmed by the electron paramagnetic resonance (EPR) spectrum (Fig. S21). Furthermore, the radical on 44bpe-PbI$_2$-P can be quenched upon heating in the air (Fig. S22). It suggests that the *tpcb* molecules can promote the generation of radical species through XLCT. Meanwhile, the optical bandgap of lead-halide CPs displays a slight increase upon photoirradiation (Fig. 5a, b, d and S22), in agreement with the decreased conjugation of *tpcb* ligands compared to the bpe ligands.[52]

In addition to the modulation of absorption spectra, solid-state [2 + 2] photocycloaddition shows a profound impact on the emission properties of lead-halide CPs. Before photo irradiation, four CPs, *i.e.*, 44bpe-PbX$_2$ (X = Cl, Br, I) and 24bpe-PbI$_2$, exhibit similar red emission spectra with three distinct vibronic structures centered at around 570, 620, and 750 nm,
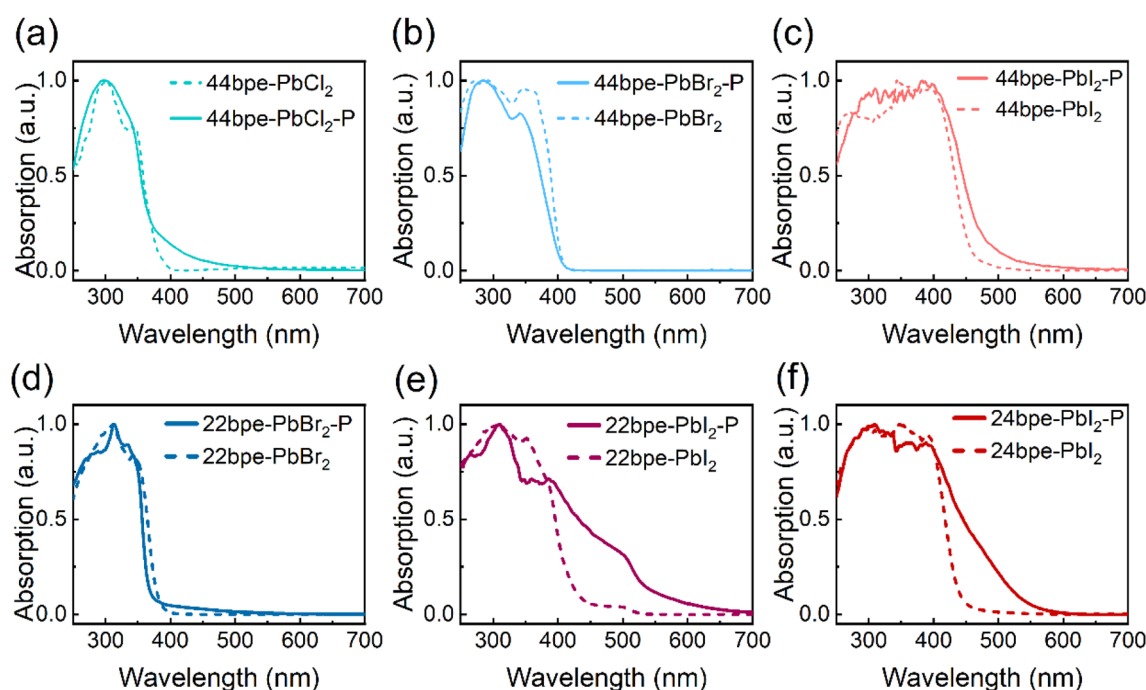

Fig. 5 Absorption spectrum changes in bpe-PbX$_2$ CPs after photocycloaddition. (a) 44bpe-PbCl$_2$. (b) 44bpe-PbBr$_2$. (c) 44bpe-PbI$_2$. (d) 22bpe-PbBr$_2$. (e) 22bpe-PbI$_2$. (f) 24bpe-PbI$_2$.
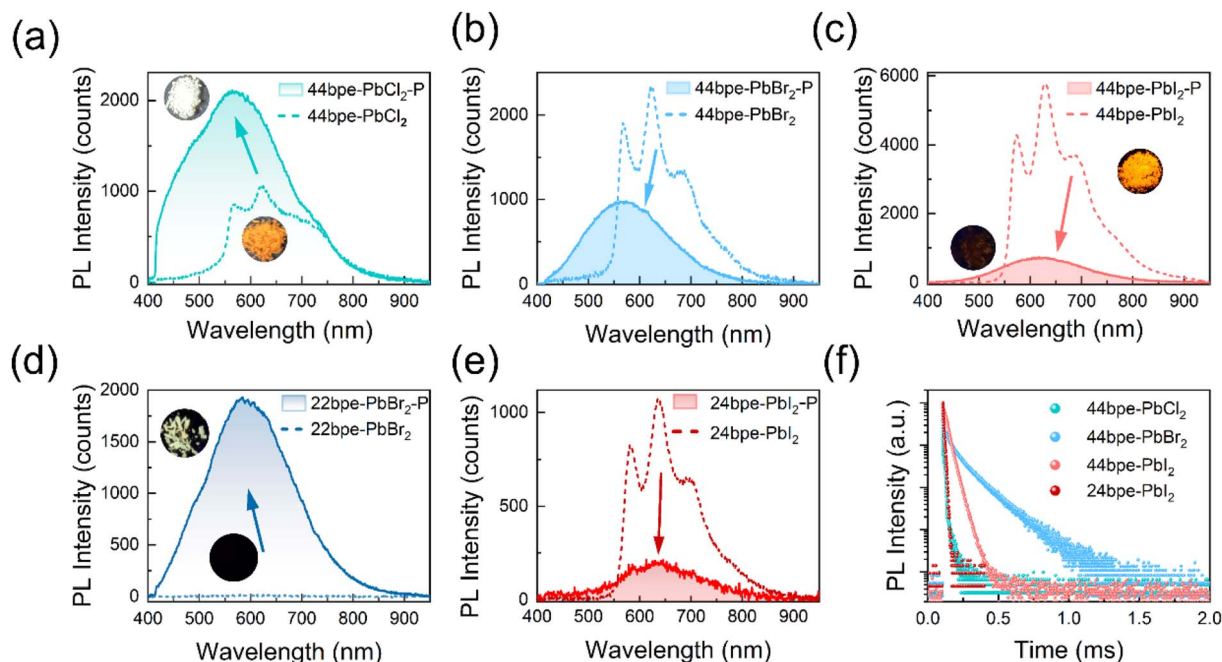
Fig. 6 Photocycloaddition-induced PL spectrum changes in 44bpe-PbCl$_2$ (a), 44bpe-PbBr$_2$ (b), 44bpe-PbI$_2$ (c), 22bpe-PbBr$_2$ (d), and 24bpe-PbI$_2$ (e). (f) PL lifetime of the bpe-PbX$_2$ CPs.

respectively (Fig. 6). These emission peaks are consistent with a previous report on lead-chloride CPs,[45] which is attributed to halide-ligand charge transfer (XLCT). The PL spectra suggest strong vibronic coupling at the excited states, akin to many organic chromophores. Their photoluminescence (PL) lifetime was measured by time-resolved PL, which gives an averaged lifetime of 1.9, 94, 32, and 7.2 µs in 44bpe-PbCl$_2$, 44bpe-PbBr$_2$, 44bpe-PbI$_2$, and 24bpe-PbI$_2$, respectively (Table S3). The microsecond lifetime indicates that the emission is attributed to phosphorescence, which is promoted by the strong SOC in the lead halides CPs. In contrast, 22bpe-PbBr$_2$ and 22bpe-PbI$_2$ are notably non-emissive at room temperature.

Interestingly, the sharp vibronic PL features of the emissive bpe-PbX$_2$ CPs become blue-shifted broadband emission after UV irradiation. For instance, 44bpe-PbCl$_2$-P displays a broadband emission spectrum ranging from 400 nm to 850 nm, with a peak centered at ~570 nm (Fig. 6a). The emission color is changed from red (CIE coordinate: 0.53, 0.43) to white light (CIE coordinate: 0.37, 0.40) (Fig. S23). The overall PL intensity increases by around two-fold after photocycloaddition. The broadband emission was also observed in 44bpe-PbBr$_2$-P, 44bpe-PbI$_2$-P, and 24bpe-PbI$_2$-P, but the PL intensity was decreased compared to the parent structure (Fig. 6b–e, also see photoluminescence quantum yields (PLQYs) in Table S3). Surprisingly, we found that the non-emissive 22bpe-PbBr$_2$ CP exhibits a yellowish emission with a broadband spectrum from 400 to 900 nm (Fig. 6d) after photocycloaddition. The average emission lifetimes of 44bpe-PbCl$_2$-P, 44bpe-PbBr$_2$-P, and 22bpe-PbBr$_2$-P were measured to be 2.7, 34, and 171 µs, respectively (Fig. S24), suggesting a phosphorescence mechanism.

To further understand the mechanism of PL modulation, we performed first-principles DFT calculations on 22bpe-PbBr$_2$ and 22bpe-PbBr$_2$-P to explore the changes in the electronic states during the photocycloaddition process. The calculated band gap is increased after photocycloaddition (Fig. S25), which agrees well with our absorption and PL measurements. For 22bpe-PbBr$_2$, the band structure shows flat valence and conduction bands, and the band-decomposed partial charge density (Fig. 7) indicates that the electron is localized on the ligand orbitals (CBM), while the hole is from the extended Pb–Br framework (VBM). This results in minimal spatial overlap between the wavefunctions associated with the VBM and CBM; according to Fermi's Golden Rule, such lack of overlap leads to a low probability for radiative transitions, accounting for the absence of PL emission in this structure. After photocycloaddition, the ligands with antibonding π* orbitals come closer, increasing their energy and facilitating hybridization with the Pb 6p–Br 4p antibonding states. In 22bpe-PbBr$_2$-P, the conduction band becomes much more dispersed, and the CBM is delocalized over both the organic ligand and the Pb–Br framework. This increased spatial overlap between the relevant orbitals enhances the probability of radiative recombination, which is consistent with the observed PL emission. This interpretation is also supported by our time-resolved PL data, where bpe-PbX$_2$-P CPs exhibit exponential (radiative) decays (Fig. S24), while bpe-PbX$_2$ CPs show linear decays (Fig. 6f), indicative of trap-assisted recombination or carrier separation. Similar behavior has been reported in other materials such as Cs$_3$Cu$_2$X$_5$ (ref. 53) and Cs$_2$AgInCl$_6$.[54] Therefore, we propose that the modulation of PL arises from changes in the ground-state electronic structure of the coordination polymers during photocycloaddition, which influences the spatial overlap of the relevant orbitals and thus the likelihood of radiative versus non-radiative recombination pathways.
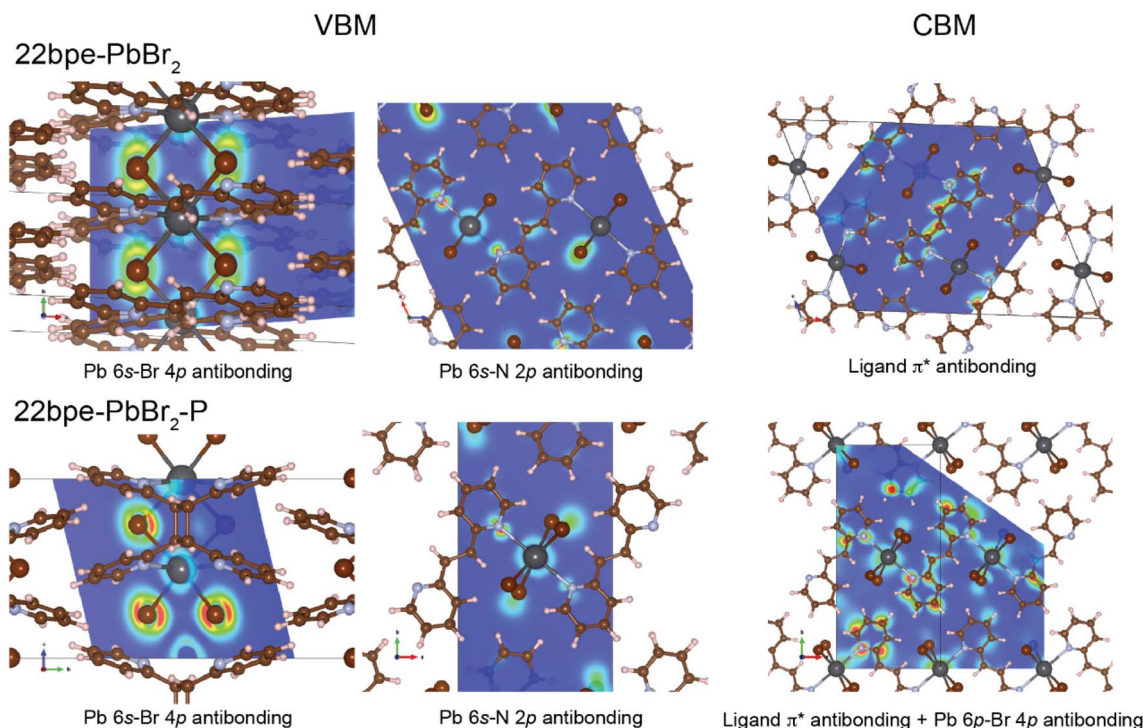
Fig. 7 Band decomposed partial charge densities of 22bpe–PbBr$_2$ (top panel) and 22bpe–PbBr$_2$–P (bottom panel) at VBM (left and middle panels) and CBM (right panel), respectively.

The longer PL lifetime and enhanced PLQY in 44bpe-PbCl$_2$-P compared to the initial structure both indicate the suppressed non-radiative decay and a dominant radiative process in it. However, the topochemical conversion nature might distort the inorganic subunits during the photocycloaddition, resulting in a more distorted inorganic lattice. This can lead to enhanced electron–phonon coupling and non-radiative relaxation through the inorganic channels.[55,56] We attribute the decreased PL intensity in 44bpe-PbBr$_2$-P, 44bpe-PbI$_2$-P, and 24bpe-PbI$_2$-P to the increased inorganic distortion after photocycloaddition (Fig. S26). We demonstrate that the post-synthetic photocycloaddition strategy can largely tune the optical properties of these bpe-based coordination polymers. The photo-responsive phosphorescence shows potential in information encryption.[43,57,58]

Conclusion

In summary, we have synthesized a series of bpe-based 2D lead-halide CPs and studied their photocycloaddition process. SCXRD results demonstrate the topochemical SCSC transformations in the CPs. We show that lead-halide CPs are a highly tunable platform to study structure–property relationships by modulating the intermolecular packing geometry and the halide composition. Our results show that the reaction rate of topochemical [2 + 2] photocycloaddition depends on the packing geometry, intermolecular distance, and the optical bandgap of CPs. Meanwhile, the stereochemistry of [2 + 2] photocycloaddition products can be readily controlled by the coordination geometry of CPs. Moreover, the photophysical properties of CPs can be modulated by the solid-state photocycloaddition. The modulation of electronic structures results in enhanced room-temperature, broadband phosphorescence in 44bpe-PbCl$_2$-P and 22bpe-PbBr$_2$-P. This work demonstrates that solid-state [2 + 2] photocycloaddition as an effective strategy to regulate the molecular structures and optoelectronic properties of bpe-based lead-halide CPs with rich chemical and structural diversity.

Experimental section

Synthesis of lead halide coordination polymers

PbBr$_2$, Pb(CH$_3$COO)$_2$, KCl, KBr, and KI were purchased from Aladin. PbBr$_2$ was purchased from Macklin. MeOH was purchased from Scharlau. 1,2-bis(4-pyridyl)ethylene (44bpe), 1,2-bis(2-pyridyl)ethylene (22bpe), and (*E*)-2-[2-(pyridin-4-yl)vinyl]pyridine (24bpe) were purchased from TCI. All the chemicals were used as received without further purification.

The synthesis of the lead halide coordination polymers was modified from the previously reported branched tube method.[42]

Synthesis of 44bpe-PbX$_2$ (X = Cl, Br, I): The 44bpe ligand (0.5 mmol) and a mixture of Pb(CH$_3$COO)$_2$ (0.5 mmol) and KX (X = Cl, Br, I) (1 mmol) were placed in the bottom of the main arm in a branched tube. MeOH was carefully added to fill both arms. The tube was sealed, and the main arm was immersed in an oil bath at 60 °C while the branched arm was kept at ambient temperature. After 3–5 days, suitable single crystals were deposited in the cooler arm due to the thermal gradient. The crystals were taken out and dried at 60 °C overnight.

Synthesis of 22pe-PbBr$_2$, 22bpe-PbI$_2$, and 24bpe-PbI$_2$: The 22bpe/24bpe ligand (0.25 mmol) and PbBr$_2$/PbI$_2$ (0.25 mmol) were placed in the bottom of the main arm in a branched tube. A mixed solution of MeOH : H$_2$O (3 : 1) was carefully added to fill both arms. The next procedure is the same as that for 44bpe-PbX$_2$.

Photocycloaddition experiment

Polycrystalline samples were uniformly placed in a small vial and irradiated under a 300 W Xe lamp for different durations of time. At each time, a portion of the sample was taken out and dissolved in (CD$_3$)$_2$SO for the NMR test. The single crystals were irradiated overnight to get the complete photocycloaddition products for further SCXRD, absorption and PL spectra characterization.

^{1}H NMR spectrum

^{1}H NMR spectra were recorded using a BRUKER AVII 400 NMR spectrometer.

Powder X-ray diffraction

The powder X-ray diffraction data were collected on a Rigaku MiniFlex powder X-ray diffractometer with a Cu K$_{\alpha 1}$/K$_{\alpha 2}$ source ($\lambda = 1.54051/1.54433$ Å).

Single crystal X-ray diffraction

Single-crystal diffraction data were collected on a Rigaku SuperNova Atlas CCD diffractometer at low temperature (173 K) using M$_O$ Kα radiation ($\lambda = 0.71073$ Å). The structures were solved by using Olex2, with the SHELXT structure solution program using Intrinsic Phasing, and the SHELXL refinement package using least squares minimization.

UV-vis absorption spectroscopy

The UV-vis absorption spectra were collected in optical diffuse reflectance mode using a UH5700 spectrophotometer with a 60 mm diameter integrating sphere. BaSO$_4$ was used as the 100% reflectance background. The crystalline samples were ground into powder and adhered to BaSO$_4$ for measurement. The Kubelka–Munk equation, $\alpha/S = (1 - R)^2/(2R)$, where R is the reflectance, α is the absorption coefficient, and S is the scattering coefficient, was applied to convert the reflectance to the absorption data.

PL spectroscopy

Temperature-dependent PL emission spectra were measured under vacuum in a sealed quartz chamber, which is cooled by liquid nitrogen. Temperature was monitored and controlled by a thermocouple connected to a temperature controller. The PL spectra were collected using a NOVA spectrometer through a confocal microscope. The sample was excited by a 365 nm UV lamp.

TRPL

The PL lifetimes were measured on an Edinburgh FLS980 photoluminescence spectrometer with excitation at 360 nm.

PLQY

Photoluminescence quantum yields (PLQYs) were measured using an integrating sphere on an Hamamatsu Quantum Yield Spectrometer C11347 Quantaurus. Data were collected three times, and the average values were reported. The PLQY was calculated using the following equation:

$$\text{PLQY} = \frac{\int I_{\text{sample}}(\lambda) - \int I_{\text{ref}}(\lambda)\text{d}\lambda}{\int E_{\text{ref}}(\lambda) - \int E_{\text{sample}}(\lambda)\text{d}\lambda}$$

where "I" indicates the measured intensity of the emitted light, "E" indicates the measured intensity of the excitation light, "sample" indicates measurements of samples, and "ref" indicates measurements of a reference (without samples).

Electron paramagnetic resonance (EPR) spectrum

EPR spectra (9.35 GHz) were recorded on a Bruker EleXsys E500 spectrometer equipped with a super-high Q resonator (ER4122SHQE) at room temperature.

Thermal analysis

Thermogravimetric analysis (TGA) was conducted on a TGA 7 PerkinElmer. The scanning rate was 10 °C min^{-1}. The test was conducted under a nitrogen atmosphere.

Author contributions

Z. C. synthesized the materials and performed photocycloaddition reactions and spectroscopic characterization studies. J. W., C. C., and L. M. collected single-crystal XRD data. B. M. and L. T. collected EPR data. Z. D. performed DFT calculations. Z. C. and H. L. wrote the manuscript. All authors discussed and analyzed the results and commented on the manuscript.

Conflicts of interest

The authors declared that they have no conflicts of interest.

Data availability

The data supporting this article have been included as part of the SI: X-ray diffraction data, ^{1}H NMR data, and more spectroscopic data (UV-vis, PL, and TRPL). See DOI: https://doi.org/10.1039/d5sc04306a.

CCDC 2407139 and 2407230–2407238 contain the supplementary crystallographic data for this paper.[59–68]

Acknowledgements

References

1 R. Z. Lange, G. Hofer, T. Weber and A. D. Schlüter, A Two-Dimensional Polymer Synthesized through Topochemical [2 + 2]-Cycloaddition on the Multigram Scale, *J. Am. Chem. Soc.*, 2017, **139**, 2053–2059.

2 C. Raju, G. R. Ramteke, K. V. J. Jose and K. M. Sureshan, Cascading Effect of Large Molecular Motion in Crystals: A Topotactic Polymorphic Transition Paves the Way to Topochemical Polymerization, *J. Am. Chem. Soc.*, 2023, **145**, 9607–9616.

3 C. L. Anderson, H. Li, C. G. Jones, S. J. Teat, N. S. Settineri, E. A. Dailing, J. Liang, H. Mao, C. Yang, L. M. Klivansky, X. Li, J. A. Reimer, H. M. Nelson and Y. Liu, Solution-processable and functionalizable ultra-high molecular weight polymers *via* topochemical synthesis, *Nat. Commun.*, 2021, **12**, 6818.

4 K. Biradha and R. Santra, Crystal engineering of topochemical solid state reactions, *Chem. Soc. Rev.*, 2013, **42**, 950–967.

5 B. B. Rath, G. Gallo, R. E. Dinnebier and J. J. Vittal, Reversible Thermosalience in a One-Dimensional Coordination Polymer Preceded by Anisotropic Thermal Expansion and the Shape Memory Effect, *J. Am. Chem. Soc.*, 2021, **143**, 2088–2096.

6 J. J. Vittal, Supramolecular structural transformations involving coordination polymers in the solid state, *Coord. Chem. Rev.*, 2007, **251**, 1781–1795.

7 J.-K. Sun, W. Li, C. Chen, C.-X. Ren, D.-M. Pan and J. Zhang, Photoinduced Bending of a Large Single Crystal of a 1,2-Bis(4-pyridyl)ethylene-Based Pyridinium Salt Powered by a [2+2] Cycloaddition, *Angew. Chem., Int. Ed.*, 2013, **52**, 6653–6657.

8 K. K. Neena, P. Sudhakar and P. Thilagar, Catalyst- and Template-Free Ultrafast Visible-Light-Triggered Dimerization of Vinylpyridine-Functionalized Tetraarylaminoborane: Intriguing Deep-Blue Delayed Fluorescence, *Angew. Chem., Int. Ed.*, 2018, **57**, 16806–16810.

9 Y. Wei, K. Chen, S. Zhu, W. Wu, H. Zhao, X. Huang, N. Wang, L. Zhou, T. Wang, J. Wang and H. Hao, Photoactuators Based on Plastically Flexible α-Cyanostilbene Molecular Crystals Driven by the Solid-State [2+2] Cycloaddition Reaction, *Small*, 2024, **20**, 2307756.

10 T. Dünnebacke, K. K. Kartha, J. M. Wahl, R. Q. Albuquerque and G. Fernández, Solvent-controlled E/Z isomerization *vs.* [2 + 2] photocycloaddition mediated by supramolecular polymerization, *Chem. Sci.*, 2020, **11**, 10405–10413.

11 G. Pan, Z. Wu, Z. Liu, B. Xu and W. Tian, Photoinduced Fluorescence Switching in Molecular Aggregates by Topological [2+2] Cycloaddition, *Angew. Chem., Int. Ed.*, 2023, **62**, e202303152.

12 J. Guo, J. Fan, X. Liu, Z. Zhao and B. Z. Tang, Photomechanical Luminescence from Through-Space Conjugated AIEgens, *Angew. Chem., Int. Ed.*, 2020, **59**, 8828–8832.

13 G. M. J. Schmidt, Photodimerization in the solid state, *Pure Appl. Chem.*, 1971, **27**, 647–678.

14 T. Kim, L. Zhu, L. J. Mueller and C. J. Bardeen, Mechanism of Photoinduced Bending and Twisting in Crystalline Microneedles and Microribbons Composed of 9-Methylanthracene, *J. Am. Chem. Soc.*, 2014, **136**, 6617–6625.

15 K. Morimoto, D. Kitagawa, F. Tong, K. Chalek, L. J. Mueller, C. J. Bardeen and S. Kobatake, Correlating Reaction Dynamics and Size Change during the Photomechanical Transformation of 9-Methylanthracene Single Crystals, *Angew. Chem., Int. Ed.*, 2022, **61**, e202114089.

16 F. Tong, M. P. Hanson and C. J. Bardeen, Analysis of reaction kinetics in the photomechanical molecular crystal 9-methylanthracene using an extended Finke–Watzky model, *Phys. Chem. Chem. Phys.*, 2016, **18**, 31936–31945.

17 A. Briceño, Y. Hill, T. González and G. Díaz de Delgado, Combining hydrogen bonding and metal coordination for controlling topochemical [2 + 2] cycloaddition from multi-component assemblies, *Dalton Trans.*, 2009, 1602–1610, DOI: 10.1039/B815149K.

18 M.-F. Wang, Y.-H. Deng, Y.-X. Hong, J.-H. Gu, Y.-Y. Cao, Q. Liu, P. Braunstein and J.-P. Lang, In situ observation of a stepwise [2 + 2] photocycloaddition process using fluorescence spectroscopy, *Nat. Commun.*, 2023, **14**, 7766.

19 T. Jadhav, Y. Fang, C.-H. Liu, A. Dadvand, E. Hamzehpoor, W. Patterson, A. Jonderian, R. S. Stein and D. F. Perepichka, Transformation between 2D and 3D Covalent Organic Frameworks *via* Reversible [2 + 2] Cycloaddition, *J. Am. Chem. Soc.*, 2020, **142**, 8862–8870.

20 T.-Y. Yu, Q. Niu, Y. Chen, M. Lu, M. Zhang, J.-W. Shi, J. Liu, Y. Yan, S.-L. Li and Y.-Q. Lan, Interpenetrating 3D Covalent Organic Framework for Selective Stilbene Photoisomerization and Photocyclization, *J. Am. Chem. Soc.*, 2023, **145**, 8860–8870.

21 R. Medishetty, I.-H. Park, S. S. Lee and J. J. Vittal, Solid-state polymerisation *via* [2+2] cycloaddition reaction involving coordination polymers, *Chem. Commun.*, 2016, **52**, 3989–4001.

22 B. B. Rath and J. J. Vittal, Single-Crystal-to-Single-Crystal [2 + 2] Photocycloaddition Reaction in a Photosalient One-Dimensional Coordination Polymer of Pb(II), *J. Am. Chem. Soc.*, 2020, **142**, 20117–20123.

23 Y. Wang, Q. Zhang, Y.-Y. Cao, Q. Liu, B. F. Abrahams and J.-P. Lang, Asymmetric reversible structural switching of

a diene coordination polymer promoted by UV-visible light, *Sci. China:Chem.*, 2024, **67**, 536–541.

24 B. B. Rath and J. J. Vittal, Photoreactive Crystals Exhibiting [2 + 2] Photocycloaddition Reaction and Dynamic Effects, *Acc. Chem. Res.*, 2022, **55**, 1445–1455.

25 X.-D. Yang, M.-J. Ma, X.-Z. Pang, Y.-R. Chen, D. Rooney and J. Zhang, Synergism of photocycloaddition and photoinduced electron transfer for multi-state responsive materials with high-stability and reversibility, *Chem. Commun.*, 2020, **56**, 4126–4129.

26 E. Hadjoudis and I. M. Mavridis, Photochromism and thermochromism of Schiff bases in the solid state: structural aspects, *Chem. Soc. Rev.*, 2004, **33**, 579–588.

27 S. Khan, Akhtaruzzaman, R. Medishetty, A. Ekka and M. H. Mir, Mechanical Motion in Crystals Triggered by Solid State Photochemical [2+2] Cycloaddition Reaction, *Chem.–Asian J.*, 2021, **16**, 2806–2816.

28 C. Raju, H. P. Q. Nguyen and G. G. D. Han, Emerging solid-state cycloaddition chemistry for molecular solar thermal energy storage, *Chem. Sci.*, 2024, **15**, 17273–17283.

29 T.-Y. Xu, F. Tong, H. Xu, M.-Q. Wang, H. Tian and D.-H. Qu, Engineering Photomechanical Molecular Crystals to Achieve Extraordinary Expansion Based on Solid-State [2 + 2] Photocycloaddition, *J. Am. Chem. Soc.*, 2022, **144**, 6278–6290.

30 S. Bhandary, M. Beliš, A. M. Kaczmarek and K. Van Hecke, Photomechanical Motions in Organoboron-Based Phosphorescent Molecular Crystals Driven by a Crystal-State [2 + 2] Cycloaddition Reaction, *J. Am. Chem. Soc.*, 2022, **144**, 22051–22058.

31 L. Wang, S.-B. Qiao, Y.-T. Chen, X. Ma, W.-M. Wei, J. Zhang, L. Du and Q.-H. Zhao, [2 + 2] cycloaddition and its photomechanical effects on 1D coordination polymers with reversible amide bonds and coordination site regulation, *Chem. Sci.*, 2024, **15**, 3971–3979.

32 R. Medishetty, A. Husain, Z. Bai, T. Runčevski, R. E. Dinnebier, P. Naumov and J. J. Vittal, Single Crystals Popping Under UV Light: A Photosalient Effect Triggered by a [2+2] Cycloaddition Reaction, *Angew. Chem., Int. Ed.*, 2014, **53**, 5907–5911.

33 R. Medishetty, S. C. Sahoo, C. E. Mulijanto, P. Naumov and J. J. Vittal, Photosalient Behavior of Photoreactive Crystals, *Chem. Mater.*, 2015, **27**, 1821–1829.

34 K. Yadava and J. J. Vittal, Solid-State Photochemical [2+2] Cycloaddition Reaction of Mn(II) Complexes, *Chem.–Eur. J.*, 2019, **25**, 10394–10399.

35 C. Sun, Y. Li, J. Yin, D. Li, C. Wu, C. Zhang and H. Fei, Highly Stable MOF-Type Lead Halide Luminescent Ferroelectrics, *Angew. Chem., Int. Ed.*, 2024, **63**, e202407102.

36 R. Xi, Y. Jiang, Y. Li, J. Yin and H. Fei, Stable self-trapped broadband emission from an organolead halide coordination polymer with strong layer corrugation and high chemical robustness, *Inorg. Chem. Front.*, 2023, **10**, 2645–2652.

37 J. Yin, X. Song, C. Sun, Y. Jiang, Y. He and H. Fei, Modulating Inorganic Dimensionality of Ultrastable Lead Halide Coordination Polymers for Photocatalytic CO2 Reduction to Ethanol, *Angew. Chem., Int. Ed.*, 2024, **63**, e202316080.

38 Z.-X. Liu, J.-Q. Wang, Y. Mu, Q. Wei, J.-H. Li and G.-M. Wang, Room-Temperature Phosphorescence with Variable Lifetime of Halogen-Comprising Coordination Polymers, *Inorg. Chem.*, 2020, **59**, 17870–17874.

39 Y.-J. Ma, Z. Qi, G. Xiao, X. Fang and D. Yan, Metal-Halide Coordination Polymers with Excitation Wavelength- and Time-Dependent Ultralong Room-Temperature Phosphorescence, *Inorg. Chem.*, 2022, **61**, 16477–16483.

40 U. Kurakula, A. Ekka, B. Dutta, M. H. Mir, N. R. Halcovitch and R. Medishetty, Photoreactive Zn(II) Coordination Compounds: Exploring Biomimetic Mechanical Motion and Photosalient Behavior, *Cryst. Growth Des.*, 2024, **24**, 7066–7074.

41 X. Liu, C. Chen, Y. Xiao, X. Li, K. Xu, X. Lian, J. Z. Zhang and B. Luo, Photocycloaddition of Zero-Dimensional Metal Halide Hybrids with Reversible Photochromism, *ACS Appl. Mater. Interfaces*, 2024, **16**, 31313–31321.

42 R. Medishetty, T. T. S. Yap, L. L. Koh and J. J. Vittal, Thermally reversible single-crystal to single-crystal transformation of mononuclear to dinuclear Zn(ii) complexes by [2+2] cycloaddition reaction, *Chem. Commun.*, 2013, **49**, 9567–9569.

43 C. Xing, Z. Qi, B. Zhou, D. Yan and W.-H. Fang, Solid-State Photochemical Cascade Process Boosting Smart Ultralong Room-Temperature Phosphorescence in Bismuth Halides, *Angew. Chem., Int. Ed.*, 2024, **63**, e202402634.

44 B. B. Rath and J. J. Vittal, Mechanical Bending and Modulation of Photoactuation Properties in a One-Dimensional Pb(II) Coordination Polymer, *Chem. Mater.*, 2021, **33**, 4621–4627.

45 X.-K. Tian, J.-R. Zhang, M.-Y. Wen, Z.-H. Liu, J.-h. Guo, C.-Y. Ma, H.-Y. Zhang, X.-G. Yang and L.-F. Ma, Red room temperature phosphorescence of lead halide based coordination polymer showing efficient angle-dependent polarized emission and photoelectric performance, *Dalton Trans.*, 2022, **51**, 10055–10060.

46 C. Sun, R. Xi and H. Fei, Organolead Halide-Based Coordination Polymers: Intrinsic Stability and Photophysical Applications, *Acc. Chem. Res.*, 2023, **56**, 452–461.

47 A. Aslani, A. Morsali, V. T. Yilmaz and O. Büyükgüngör, 2D Holodirected lead(II) bromide coordination polymers constructed of rigid and flexible ligands, *Inorg. Chim. Acta*, 2009, **362**, 1506–1510.

48 Y. Li, J. Yin and H. Fei, Lead Halide Hybrids Templated by Two Coordinating Ligands for Enhanced and Stable Self-Trapped Emission, *Inorg. Chem.*, 2023, **62**, 19804–19811.

49 Z.-Y. Yang, X. Sang, D. Liu, Q.-Y. Li, F. Lang, B. F. Abrahams, H. Hou, P. Braunstein and J.-P. Lang, Photopolymerization-Driven Macroscopic Mechanical Motions of a Composite Film Containing a Vinyl Coordination Polymer, *Angew. Chem., Int. Ed.*, 2023, **62**, e202302429.

50 A. Briceño, D. Leal, R. Atencio and G. Díaz de Delgado, Supramolecular isomerism in multivalent metal-templated assemblies with topochemical influence in the regioselective synthesis of tetrakis(2-pyridyl)cyclobutane

isomers, *Chem. Commun.*, 2006, 3534–3536, DOI: **10.1039/B606673A**.

51 C. Cao, X.-R. Xue, Q.-Y. Li, M.-J. Zhang, B. F. Abrahams and J.-P. Lang, Phase Transition-Promoted Rapid Photomechanical Motions of Single Crystals of a Triene Coordination Polymer, *Angew. Chem., Int. Ed.*, 2023, **62**, e202306048.

52 S. Islam, J. Datta, S. Maity, B. Dutta, S. Khan, P. Ghosh, P. P. Ray and M. H. Mir, Photodimerization of a 1D Ladder Polymer through Single-Crystal to Single-Crystal Transformation Has an Effect on Electrical Conductivity, *Cryst. Growth Des.*, 2019, **19**, 4057–4062.

53 L. Lian, M. Zheng, P. Zhang, Z. Zheng, K. Du, W. Lei, J. Gao, G. Niu, D. Zhang, T. Zhai, S. Jin, J. Tang, X. Zhang and J. Zhang, Photophysics in $Cs_3Cu_2X_5$ (X = Cl, Br, or I): Highly Luminescent Self-Trapped Excitons from Local Structure Symmetrization, *Chem. Mater.*, 2020, **32**, 3462–3468.

54 J. Luo, X. Wang, S. Li, J. Liu, Y. Guo, G. Niu, L. Yao, Y. Fu, L. Gao, Q. Dong, C. Zhao, M. Leng, F. Ma, W. Liang, L. Wang, S. Jin, J. Han, L. Zhang, J. Etheridge, J. Wang, Y. Yan, E. H. Sargent and J. Tang, Efficient and stable emission of warm-white light from lead-free halide double perovskites, *Nature*, 2018, **563**, 541–545.

55 X. Gong, O. Voznyy, A. Jain, W. Liu, R. Sabatini, Z. Piontkowski, G. Walters, G. Bappi, S. Nokhrin, O. Bushuyev, M. Yuan, R. Comin, D. McCamant, S. O. Kelley and E. H. Sargent, Electron–phonon interaction in efficient perovskite blue emitters, *Nat. Mater.*, 2018, **17**, 550–556.

56 W. Chen, Y. Shi, J. Chen, P. Ma, Z. Fang, D. Ye, Y. Lu, Y. Yuan, J. Zhao and Z. Xiao, Polymerized Hybrid Perovskites with Enhanced Stability, Flexibility, and Lattice Rigidity, *Adv. Mater.*, 2021, **33**, 2104842.

57 Z. Han, M. He, G. Wang, J.-M. Lehn and Q. Li, Visible-Light-Driven Solid-State Fluorescent Photoswitches for High-Level Information Encryption, *Angew. Chem., Int. Ed.*, 2024, **63**, e202416363.

58 M. He, C. Ding, Z. Han, T. Liang, H. Guo, Z. Liu and Q. Li, Visible-Light-Driven [2+2] Photocycloaddition in Self-Assembled State for Time-Resolved Information Encryption, *Adv. Opt. Mater.*, 2025, 2403525.

59 Z. Chen, J. Wu, Z. Deng, C. Chen, J. Feng, B. Ma, L. Tao, L. Mao and H. Lu, CCDC 2407139: Experimental Crystal Structure Determination, 2025, DOI: **10.5517/ccdc.csd.cc2lstnw**.

60 Z. Chen, J. Wu, Z. Deng, C. Chen, J. Feng, B. Ma, L. Tao, L. Mao and H. Lu, CCDC 2407230: Experimental Crystal Structure Determination, 2025, DOI: **10.5517/ccdc.csd.cc2lsxlx**.

61 Z. Chen, J. Wu, Z. Deng, C. Chen, J. Feng, B. Ma, L. Tao, L. Mao and H. Lu, CCDC 2407231: Experimental Crystal Structure Determination, 2025, DOI: **10.5517/ccdc.csd.cc2lsxmy**.

62 Z. Chen, J. Wu, Z. Deng, C. Chen, J. Feng, B. Ma, L. Tao, L. Mao and H. Lu, CCDC 2407232: Experimental Crystal Structure Determination, 2025, DOI: **10.5517/ccdc.csd.cc2lsxnz**.

63 Z. Chen, J. Wu, Z. Deng, C. Chen, J. Feng, B. Ma, L. Tao, L. Mao and H. Lu, CCDC 2407233: Experimental Crystal Structure Determination, 2025, DOI: **10.5517/ccdc.csd.cc2lsxp0**.

64 Z. Chen, J. Wu, Z. Deng, C. Chen, J. Feng, B. Ma, L. Tao, L. Mao and H. Lu, CCDC 2407234: Experimental Crystal Structure Determination, 2025, DOI: **10.5517/ccdc.csd.cc2lsxq1**.

65 Z. Chen, J. Wu, Z. Deng, C. Chen, J. Feng, B. Ma, L. Tao, L. Mao and H. Lu, CCDC 2407235: Experimental Crystal Structure Determination, 2025, DOI: **10.5517/ccdc.csd.cc2lsxr2**.

66 Z. Chen, J. Wu, Z. Deng, C. Chen, J. Feng, B. Ma, L. Tao, L. Mao and H. Lu, CCDC 2407236: Experimental Crystal Structure Determination, 2025, DOI: **10.5517/ccdc.csd.cc2lsxs3**.

67 Z. Chen, J. Wu, Z. Deng, C. Chen, J. Feng, B. Ma, L. Tao, L. Mao and H. Lu, CCDC 2407237: Experimental Crystal Structure Determination, 2025, DOI: **10.5517/ccdc.csd.cc2lsxt4**.

68 Z. Chen, J. Wu, Z. Deng, C. Chen, J. Feng, B. Ma, L. Tao, L. Mao and H. Lu, CCDC 2407238: Experimental Crystal Structure Determination, 2025, DOI: **10.5517/ccdc.csd.cc2lsxv5**.